

In Situ Synchrotron Powder Diffraction Study of Cd Intercalation into Chevrel Phases Crystal Structure and Kinetic Effect

José Barbosa, Carmelo Prestipino, Olivier J Hernandez, Serge Paofai, Catherine Dejoie, Maryline Guilloux-Viry, Clotilde Boulanger

▶ **To cite this version:**

José Barbosa, Carmelo Prestipino, Olivier J Hernandez, Serge Paofai, Catherine Dejoie, et al.. In Situ Synchrotron Powder Diffraction Study of Cd Intercalation into Chevrel Phases Crystal Structure and Kinetic Effect. Inorganic Chemistry, 2019, 58 (3), pp.2158-2168. 10.1021/acs.inorgchem.8b03259 . hal-02019479

HAL Id: hal-02019479

https://univ-rennes.hal.science/hal-02019479

Submitted on 22 Mar 2019

HAL is a multi-disciplinary open access archive for the deposit and dissemination of scientific research documents, whether they are published or not. The documents may come from teaching and research institutions in France or abroad, or from public or private research centers.

L'archive ouverte pluridisciplinaire **HAL**, est destinée au dépôt et à la diffusion de documents scientifiques de niveau recherche, publiés ou non, émanant des établissements d'enseignement et de recherche français ou étrangers, des laboratoires publics ou privés.

In situ synchrotron powder diffraction study of Cd intercalation into Chevrel phases: crystal structure and kinetic effect

José Barbosa[1], Carmelo Prestipino[2], Olivier J. Hernandez[2*], Serge Paofai[2], Catherine Dejoie[3], Maryline Guilloux-Viry[2], Clotilde Boulanger[1]*

[1] CEM/CP2S, Institut Jean Lamour, UMR CNRS 7198, Université de Lorraine, 1 boulevard Arago 57078 Metz, France

[2] Univ Rennes, CNRS, ISCR (Institut des Sciences Chimiques de Rennes) - UMR 6226, 35000 Rennes, France

[3] ESRF, 71 avenue des Martyrs, CS 40220, 38043 Grenoble Cedex 9, France

[*] carmelo.prestipino@univ-rennes1.fr, olivier.hernandez@univ-rennes1.fr

Accepted Manuscript

Abstract

Chevrel phases are molybdenum chalcogenides of formula $M_xMo_6X_8$ (M is a cation and X a chalcogen) that present a complex and captivating intercalation chemistry that has drawn the interest of the solid state chemistry community since their discovery [1–3] . This property has a huge potential for applied science and device development for energy storage [4], pollutants removal or detection[5,6] , but a deeper knowledge of the intercalation processes and chemistry is still necessary. In the present work, the intercalation of Cd^{2+} in aqueous solution has been studied taking advantage of the complementarity of electrochemistry characterization and synchrotron powder diffraction, acquired during an *in situ* combined experiment. During the experiment, industrially adequate electrochemical conditions (room temperature and reduced process time) have been applied, allowing a better understanding of the intercalation processes. The intercalated phases obtained by electrochemistry have been characterized *ex situ*, and for the first time, the structures of $Cd_2Mo_6X_8$ (X=S, Se) have been determined.

Unexpectedly, $Cd_2Mo_6Se_8$ presents a trigonal crystal structure with only cavity 2 occupied, which has not been encountered before for Chevrel phases.

KEYWORDS

Chevrel phases, Cd removal, powder diffraction, electrochemistry

Introduction

$M_xMo_6X_8$ and the binary compounds Mo_6X_8 belong to the family of insertion materials called Chevrel phases, that are of great interest for numerous purposes, in relation with their high ionic mobility[7]. The electrochemical intercalation of different cations (Mg^{2+}, Ni^{2+}, Cu^{2+}, Zn^{2+}, Cd^{2+}…) has already been demonstrated in the Mo_6X_8 host matrix[5,8,9], and presents an important potential for numerous applications. For instance, Mo_6S_8 thin films have been proven as an accurate sensor for the detection and quantification of hazardous elements [10], and Mo_6S_8 is a promising candidate as cathode material for the development of high performance rechargeable batteries [11,12] , with particularly interesting results for Mg batteries [4,13,14].

Among the several potential applications, the Electrochemical Transfer Junction (ETJ) method for cadmium removal, proposed C. Boulanger *et al.* [5,15,16], seems very promising. Cadmium (Cd) is a rare metallic element and its natural occurrence in the environment is always low (< 1 mg kg^{-1})[17], higher concentration levels result mainly from anthropogenic activities such as mining, smelting, metal plating, battery, waste disposal, or the application of phosphate fertilizers[18]. The accumulation in soil and in the food chain generate a critical world-wide problem, being Cd highly toxic for plants[19] and animals, and contaminated products consumption results in serious human diseases[20]. For such reasons, several methods for the treatment of industrial wastewater have been developed[21], among them ETJ presents as advantages a high selectivity in cations removal but also the possibility to easily recuperate the removed cations with clear economic benefit for high valuable elements, as Co. The electrochemical process is based on the use of a Mo_6X_8 matrix as mineral junction between two half-cells[5], one containing the contaminated solution and the other the accumulation solution.

However, such technique has not been industrially applied to the removal of Cd^{2+} atoms yet and one of the possible explanations of such retard is the incertitude in the chemistry of Cd

Accepted Manuscript

intercalation in Mo_6X_8 and its selectivity. Indeed, although the reaction has been already studied by Boulanger *et al.* [8,22] and by Gocke *et al.* [23] the results are still not clear and remain subject to reinterpretation[7]. Effectively, Gocke *et al.*[23] observed two potential plateau regions for Mo_6Se_8 and only one for MoS_8 during Cd^{2+} galvanostatic intercalation in an aqueous electrolyte solutions. Such observation, with the support of *ex situ* crystallographic cell parameters evaluation have been interpreted by the existence of two line-phases for the Mo_6Se_8 ($CdMo_6Se_8$ and $Cd_2Mo_6Se_8$) and only one-line phase for Mo_6S_8 ascribed to $CdMo_6S_8$. Boulanger *et al.*[8] by cyclic voltammetry, confirmed the interpretation for Mo_6Se_8 but underlined some discrepancies in the case of Mo_6S_8. Although the experiment was in agreement with the existence of a single step intercalation process, the authors noticed that the initial stoichiometry $CdMo_6S_8$ could be enriched till $Cd_2Mo_6S_8$ by imposing the potential of the cathodic peak. Finally, such interpretation for S has been questioned by Levi on the basis of similitudes in respect to other cation intercalation for Mo_6X_8 phases [7].

Clearly a better knowledge of thermodynamic, kinetic and selectivity of intercalation electrochemistry would improve the development and industrialization of the ETJ technology. The understanding of the evolution of the phases with the potential, apart to represent a further step toward a more general comprehension of the interaction chemistry of Mo_6X_8 phases and a significant stage for future investigations, will allow to understand the evolution of materials during applications and prevent heterogeneous transformation, as proven by the several studies coupling structural techniques with electrochemistry [3,24–27]. However, on a more fundamental point of view, the *condicio sine qua non* to determine the atomistic origin of the intercalation chemistry and high mobility of Chevrel phases is a complete structural characterization of the intercalation compounds as proven by Levi *et al.* [7,28].

In this study, we report an *in situ* coupled electrochemistry and synchrotron powder diffraction study of the intercalation and de-intercalation of Cd^{2+} in Chevrel phases Mo_6X_8 (X=S, Se) in order to elucidate the intercalation processes (and possible pitfall in the galvanostatic intercalation experiment for these materials) and the structural determination of the phases obtained during the electrochemistry processes.

Experimental

Mo_6X_8 phases were synthesized by solid state reaction. $Ni_{1.7}Mo_6S_8$ was first prepared via solid-state synthesis from a stoichiometric mixture of nickel (99.7%, Sigma-Aldrich), molybdenum (99.9%, Sigma-Aldrich), and molybdenum sulfide (99.98%, Sigma-Aldrich) at

Accepted Manuscript

1150 °C for 48 h in a vacuum-sealed fused-silica tube. Then, Mo_6S_8 was obtained via nickel-ion extraction (oxidation) from $Ni_{1.7}Mo_6S_8$ by stirring the powder overnight in a $HCl{\cdot}H_2O$ (50:50) solution, followed by suction filtration, distilled water washing, and finally drying at 100°C in an oven for 24 h. Energy-dispersive X-ray spectroscopy (EDS) probe during SEM characterization and Cyclic Voltammetry show no residual trace of Nickel in the powder. Mo_6Se_8 is directly obtained by mixing the molybdenum (99.9%, Sigma-Aldrich), and molybdenum selenide (99.98%, Sigma-Aldrich) in stoichiometric quantities. The reagents were sealed in a Mo crucible and heated at 1300°C for 48 h.

Electrochemical measurements has been performed in a three-cell electrode at ambient temperature using as reference a commercial Ag/AgCl electrode (Bioblock) in aqueous electrolytes $CdSO_4$ 0.1 M ($CdSO_4{\cdot}8/3H_2O$, Roth, purity >99%). Electrochemical experiments were conducted on an Autolab PGSTAT204 controlled by Nova software with calibrated electrode with a 10 mV precision. For the current densities the precision is equal to 0.2 %. Cyclic voltammetry (CV) sweep started from the open-circuit voltage (OCV) to negative potentials, sweep rate used being of 0.01 and 1 mV/s. The potential limits were set from -1 V (to avoid metal deposition and water reduction) to 0.3 V the limit of oxidation stability of the Mo_6X_8 phases.

Combined synchrotron X-ray powder diffraction and electrochemistry measurements have been performed in an *ad hoc* conceived electrochemical cell equipped by a working electrode aligned with the center of the two circle diffractometer, a reference electrode composed by Pt wire enrolled in spiral, and an Ag/AgCl reference electrode (all the potentials will be expressed in this potential scale). In order to avoid gradient concentrations of Cd during experiment, the electrolyte solution has been continuously refreshed in the cell by the use of a peristaltic pump. A scheme of the setup is drawn in figure S1 of the supplementary materials.

In order to avoid strong X-ray absorption effects, the working electrode containing Mo_6X_8 has been designed with the constraint of a maximum thickness of 100 µm. The working electrode was built using a Pt-wire enrolled in a spiral with an hole in the middle, coated with a slurry composed by a mix of Mo_6X_8 (X=S; Se) powder, and a polyvinylidene difluoride, (PVDF) binder (W#1300, Kureha Co.) (9:1 weight ratio), dispersed in carbonate propylene at 80°C. The electrode was finally dried at 60 °C for 72 hours, and at this stage the hole in the center was covered by a thin film of Mo_6X_8-PVDF in electronic contact with the wire, allowing the X-ray beam to pass without the interference with Pt. Each electrode was loaded with 15 mg of

Accepted Manuscript

Mo_6X_8 over an area of about 1 cm^2, however such loading should be considered as nominal due to the possibility of a residual fraction of PVDF (< 10%) still present in the sample. The experiments were performed at the high resolution powder diffraction beamline ID22 at ESRF. The source of the beamline is a double undulator, with variable gap, and the emission is monochromatized by a Si (111) channel cut monochromator. The photons scattered have been collected by 9 scintillation detectors preceded by 9 Si (111) analyzer [29] crystals. A wavelength of 0.354170 Å has been selected in order to minimize sample environment parasitic signals still maintaining a good resolution. During the *in situ* experiments, in order to obtain a more general description, for each acquisition the electrochemical cell has been translated, sampling three different positions of the working electrode. Consequently, each acquisition is the average of three individual scans of 5.5 minutes going from 0.5° to 33° 2θ ($d_{min} \approx 0.63$ Å). The use of very thin electrodes combined with the high resolution configuration and the absence of sample movement (i.e. rotation) resulted in a poor grain orientation statistics strongly affecting the relative intensity of the different reflections. The existence of such inconvenient, that prevent a proper Rietveld analysis of *in situ* data, is proven by the strong difference between the signal collected by each of the nine detectors, the impossibility to perform a physically sensible fit and the large difference between patterns collected for the same sample in *in situ* configuration in respect to optimal rotating capillary configuration (i.e. *ex situ*).

For such reasons, the *in situ* data have been treated in the approximation of the crystallites composing the electrode don't change orientation significantly, the fraction of the different phases has been evaluated by the integrated intensity of an isolated specific reflection for the three phases scaled by the square of structure factor calculated from the corresponding crystal structure. Such procedure has been performed by the use of sequential Rietveld refinements, as coded in the FullProf code [30] but limiting the refinement to the three ranges in which the selected reflection (using hexagonal setting (211) and (101) reflections for $Cd_xMo_6Se_8$ and $Cd_xMo_6S_8$, respectively) for all Chevrel phases fall and to constrain the structural parameters to the values obtained by ex situ characterization.

In view of performing accurate Rietveld refinements, complementary experiments were carried out *ex situ* on the binary Mo_6X_8 and on powders obtained from laboratory electrochemistry experiments, using a rotating borosilicate glass capillary of 0.3 mm in diameter and higher counting statistics (around 1 hour for each sample). Rietveld refinements for *ex situ* investigations have been performed by the use of Jana [31] software for the structure

Accepted Manuscript

refinement and the localization of Cd ions, applying cylindrical absorption correction as implemented in the code using a packing fraction of 0.5 and calculated density. The regions with the few low intensity spurious peaks, ascribed to impurities, were excluded from the fit, in order to obtain more reliable refinements convergence and representative agreement factors. During refinement background has been modelled by a twenty five terms Chebyshev polynomial, and peaks profiles have been modelled by pseudo Voigt functions, further details could be retrieved in the CIF files. Maximum entropy method (MEM) calculations using observed intensity and phasing obtained by Rietveld refinement have been performed by the means of the Dysnomia code [32].

The structures for $Cd_xMo_6X_8$ have been determined from two samples that were biphasic, for X=S $Cd_1Mo_6S_8$: 75.0(7) wt% $Cd_2Mo_6S_8$: 25.0(15) wt% and for X= Se $Cd_1Mo_6Se_8$: 40(1) wt%; $Cd_2Mo_6Se_8$: 60(1) wt%. The results obtained by ex-situ refinements have been graphically represented with the help of the Vesta software[33].

Scanning Electron Microscopy (SEM) images of Mo_6Se_8 and Mo_6S_8 were collected at 30 kV with a Tescan Vega 3 microscope, in secondary electron imaging mode.

Results and discussion

Pristine materials characterization

Synthesized Mo_6Se_8 and Mo_6S_8 phases have been characterized by *ex situ* synchrotron radiation Rietveld refinement, confirming results obtained from laboratory diffractometers and absence of Nickel residual trace in Mo_6S_8. The crystal structure of both phases is trigonal with space group $R\bar{3}(148)$, and lattice parameters for hexagonal setting (*hP*) a = 9.565247(15) Å and c = 11.17121(2) Å for the Se phase and a = 9.193645(14) Å and c = 10.89027(2) Å for the S phase corresponding in the rhombohedral setting (*hR*) to a=6.6606(1) Å, α=91.79(1)° and a=6.4305(1) Å, α= 91.26(1)° for Se and S respectively. As expected, Mo_6Se_8 presents a larger cell volume than Mo_6S_8 (885.163(3) *versus* 797.158(2) $Å^3$) due to a larger atomic radius of Se with respect to S, 1.20 Å *versus* 1.05 Å, respectively[34]. The refined atomic parameters and selected interatomic distances for both phases are summarized in supplementary materials and are in good agreement with previous reports[1,7,22,28,35]. However, due to the high counting statistics and resolution of synchrotron powder diffraction,

Accepted Manuscript

few spurious peaks have been detected ascribed to minor impurity phases (lower than 1 %) such as $MoSe_2$ and MoS_2, and probably few cluster condensed phases not detected during preliminary powder characterization. Analysis of peaks broadening using profile coefficients from the Rietveld refinement shows a small isotropic broadening due to internal strain (average max-strain $7.43(3)\times10^{-4}$ and $6.02(3)\ 10^{-4}$ for Mo_6Se_8 and Mo_6S_8, respectively) while broadening due to crystallite size has been only detected for Mo_6S_8 with an average size of 3.06(1) μm. SEM images support XRD evaluation, both materials showing grains with irregular parallelepiped shape with a larger dimension for Mo_6Se_8 than for Mo_6S_8, from 10 to 30 μm for the former and few μm for the latter (Figure S2 part c and d).

Accepted Manuscript

Cyclic voltammetry

Mo_6Se_8

In figure 1 part a) is shown the cyclic voltammetry of Mo_6Se_8 at 0.01 mV/s in an aqueous solution of $CdSO_4$ 0.1 M. The voltamperogram is characterized by two intercalation peaks E_{int1} and E_{int2} (around 0.35 V and -0.52 V) and two de-intercalation peaks E_{deint1} and E_{deint2} (around - 0.42 V and -0.25 V), in agreement with the literature[8,36]. In accordance with the works of Boulanger *et al*[8] the first peak is ascribed to the intercalation of a single Cd^{2+}:

$$Mo_6X_8 + Cd^{+2} + 2e^- \rightarrow CdMo_6X_8 \quad (1),$$

while the second peak corresponds for the selenide phase to the intercalation of the second Cd^{2+}:

$$CdMo_6X_8 + Cd^{2+} + 2e^- \rightarrow Cd_2Mo_6X_8 \quad (2).$$

Both reactions are reversible and the ionic transfer is mainly limited by cation diffusion in the solid, with the first insertion showing a cation diffusion slower than the second due to the different broadening of the peaks when potential sweep rate is changed[8,36]. However, differently from previous experiments when the cyclic voltammetry is performed with a sweeping rate of 1 mV/s or higher (Figure 1 part b), a new peak (E_{inta}) appears at intermediate values between the first and second intercalation peak. The nature of this intermediate peak will be discussed later with the support of *in situ* structural investigations as cyclic voltammetry alone is not sufficient to ascribe this peak.

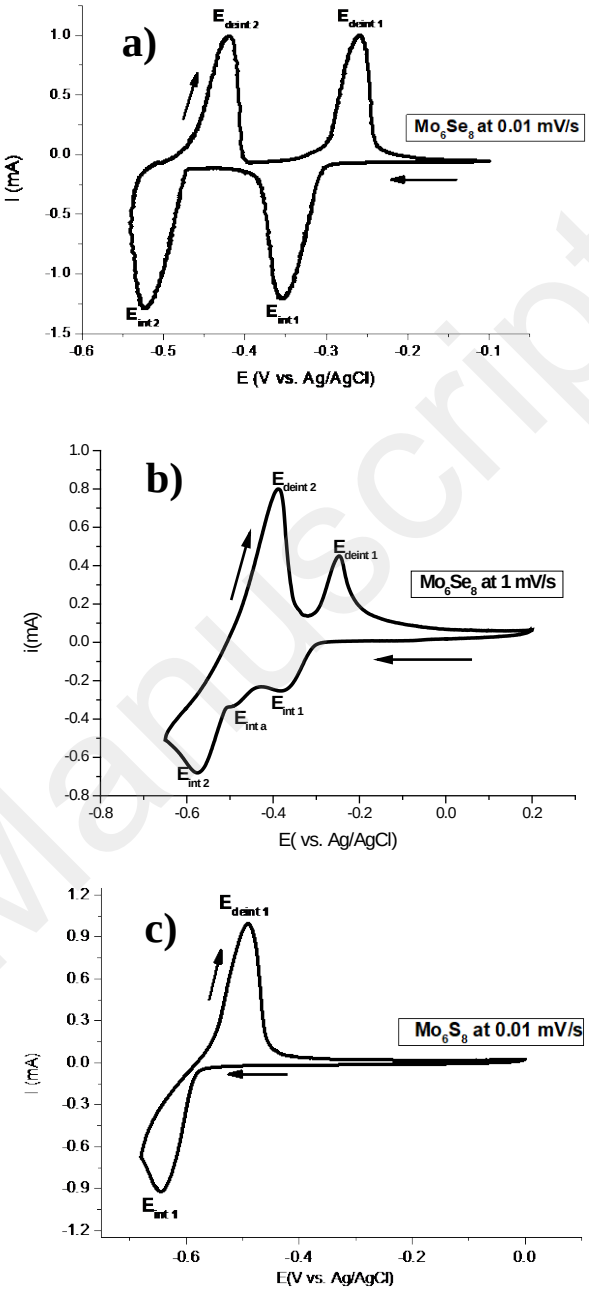


Figure 1 : cyclic voltammetry of part a) and b Mo_6Se_8 at two different cycling rate part c) of Mo_6S_8 with the rate 0.01 mV/s for 0.1 M solutions of Cd^{2+};

Accepted Manuscript

Mo_6S_8

Mo_6S_8 cyclic voltammetry is clearly different from $MoSe_8$, the voltamperogram (Figure 1 part c)) exhibits only one intercalation peak and one de-intercalation signal (at -0.62 V and -0.49 V) independently from the sweep rate. According to the literature[8,23,37], the assignment of such peaks is debated among the reaction (1) or reaction (2).

Galvanostatic intercalation

The intercalation reactions observed by cyclic voltammetry have been investigated *in situ* by coupled diffraction/electrochemistry experiments in galvanostatic mode *i.e.* imposing a fixed current and monitoring the potential variation necessary to counterbalance the change in resistance of the system, following intercalation/deintercalation processes. Such approach, focused on the thermodynamics of the reaction, is very widespread for combined XRD/ electrochemical experiment [2,3,23–27] because it has the advantage to promote reactions in the bulk and not limited to the surface of the electrode (as CV). Moreover, although this technique doesn't allow a kinetic modeling of the reactions, it allows to directly relate the type of reaction with the shape of potential evolution with a clear complementarity with structural techniques[38].

*Selenium phases***:**

A typical series of diffraction patterns taken during an intercalation cycle is shown in Figure 2 a), displaying in the inset a zoom at low angles around reflection (100) in *hR* setting of binary Mo_6Se_8. The patterns could be deconvoluted as the sum of up to three contributions, the initial binary Mo_6Se_8 phase (space group $R\bar{3}$, a=9.543, c= 11.17 Å), a first rhombohedral intercalated phase (space group $R\bar{3}$, a = 9.76, c =11.20 Å) that is ascribed to $CdMo_6Se_8$[28] , and a second rhombohedral ternary phase (space group $R\bar{3}$, a=10.2489, c=10.8789 Å) that has been previously ascribed to $Cd_2Mo_6Se_8$[36], but whose structure is still unknown. A more clear correlation between stoichiometry and cells metric could be noticed adopting the rhombohedral setting, insertion of cations generate an elongation of the packing and an

Accepted Manuscript

increase of the trigonal distortion (Mo_6Se_8 *a* = 6.65 Å, α= 91.7°, $CdMo_6Se_8$ *a* = 6.76 Å, α= 92.44°, $Cd_2Mo_6Se_8$ *a* = 6.94 Å, α= 95.19°).

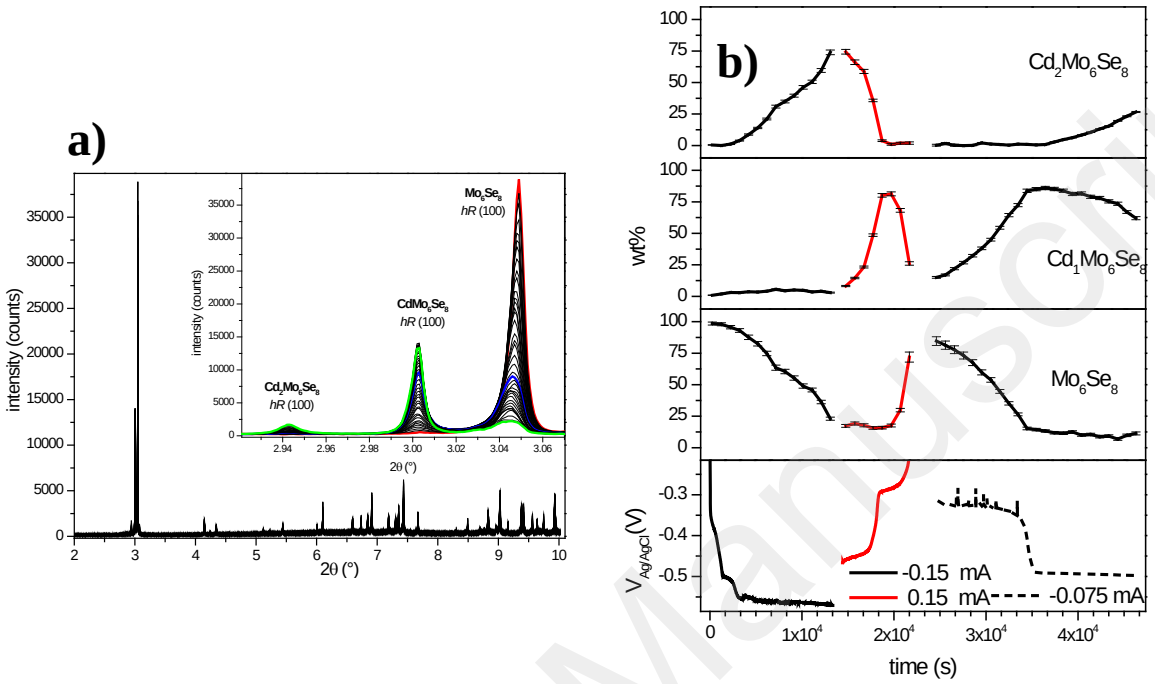


Figure 2: part a) *In situ* diffraction pattern during galvanostatic intercalation in Mo_6Se_8: part a) typical pattern (inset: zoom around the reflection of the different phases during the first intercalation stage); part b) from to top to bottom: estimated phase fractions and corresponding voltage evolution as a function of time.

In Figure 2 b) the evolution of the weight fractions of the phases associated with the potential evolution during a galvanostatic cycle is shown. During the intercalation process, in the initial stage of reduction (t <50 s,), the potential decreases rapidly in the range between 0 and -0.35 V with negligible change in XRD patterns, such abrupt variation being typical for galvanostatic electrochemistry experiment and generally associated to small deterioration of the electrode or other parasitic currents. As a consequence, the real first stage of reaction is between 50 and 1350 s with an apparent single phase reaction region, *i.e.* a region with continuous and monotone potential variation, where the potential pass from -0.35 to -0.50 V which corresponds in accordance with CV to the potential of the first insertion of Cd in the structure. However, the inspection of the diffraction data shows clearly that it is rather a two-phase region with the appearance and increase of the peaks associated to $Cd_1Mo_6Se_8$.

Accepted Manuscript

A second intercalation stage is present between 1350 and 2820 s (0.14 e^-/mol) where the potential remains almost constant at around -0.50 V. This region, from an electrochemistry point of view, due to the constant potential, presents a clearer two-phase character and could be ascribed to the second intercalation peak **E**i**nt$_a$** presents on the CV in fast sweeping condition. From a structural point of view, the intercalation mechanism is not clear, due to the insufficient time resolution of XRD acquisition. In the interval of just one data acquisition of 16.5 min, several processes mixed together, inducing a small increase of $Cd_1Mo_6Se_8$, a clear increase of $Cd_2Mo_6Se_8$ and a strong decrease of the original Mo_6Se_8 phase.

The final stage of intercalation occurs between 3000 and 13350 s where a second zone with a constant potential (-0.56 V) is present along with a clear decrease of Mo_6Se_8, specular to the increase of $Cd_2Mo_6Se_8$, as visible in Figure 2b, meanwhile the $Cd_1Mo_6Se_8$ XRD peak remains rather unchanged. On the basis of the structural results and cyclic voltammetry, this process should be related to the direct intercalation of 2 Cd^{2+} atoms within the binary grains, as described in the reaction (3)

$$Mo_6X_8 + 2Cd^{2+} + 4e^- \rightarrow Cd_2Mo_6X_8 \quad (3)$$

The de-intercalation process has been studied on the same sample just by inverting the current flow (red curve in Figure 2 b). De-intercalation is limited to only a minority part of the sample before the potential rises to high values. The de-intercalation process could be divided in two double phase transformation regions: a first region from 14370 to 17670 s with a potential at 0.45 V and a second from 18500 to 21100 s at -0.28 V corresponding to the two peaks present in the deintercalation electrochemical signal of Figure 1a. In the first region of de-intercalation, the decrease in intensity of the peaks ascribed to $Cd_2Mo_6Se_8$ is concomitant with the increase of the ones of $Cd_1Mo_6Se_8$ (the binary XRD peaks remaining almost constant in intensity), leading to the almost complete disappearance of the $Cd_2Mo_6Se_8$ phase, so this de-intercalation step could be ascribed to the inverse of reaction 2; during the second step of de-intercalation, peaks ascribed to $Cd_1Mo_6Se_8$ decreases accompanied by an increase of the intensity of peaks associated to the binary phase following the inverse of reaction (1). It should be underlined that the binary phase obtained presents a peculiar peak profile with a pronounced asymmetry on the left that could be caused by experimental inconvenience such as a gas bubble standing in front of the beam or by the existence of very strained additional phase parent of the initial Mo_6Se_8 (Figure S3).

Accepted Manuscript

In order to better investigate the intercalation steps after the de-intercalation process, a further intercalation process has been repeated on the same electrode, but with a lower imposed current of -0.075 mA (dashed black curve on figure 2 b). The lower current has two effects: (i) it avoids the polarization of the electrode due to the low ionic conductivity; (ii) it allows a better reaction sampling. Such second intercalation process presents a simpler electrochemical profile with respect to the precedent, with two double phase regions. The first one at a potential of -0.32 V that could be associated by XRD to reaction (1) while the second at around -0.50 V that should be linked to a mechanism involving the transformation of Cd_1MoSe_8 into Cd_2MoSe_8 as described by reaction (2).

It is worth underlining, that for Mo_6Se_8, the limited rate of intercalation and deintercalation reaction affects chronovoltametry with large imposed current as well as CV for rapid sweeping, revealing interesting kinetic effects. In the hypothesis that solid state diffusion is the limiting step for the intercalation and that the diffusion of Cd^{2+} in Chevrel phases depends on the concentration of Cd^{2+} within the phase, the higher the concentration, the faster the diffusion [7], we could propose the following interpretation to explain the results during intercalation reaction in Mo_6Se_8:

For slow intercalation (present experiment 0.075 mA for chronopotentiometry and 0.01 mV/s for CV**)**. During galvanostatic intercalation, if the current imposed is lower than the maximal possible diffusion of Cd^{+2} in Mo_6Se_8, the reaction proceeds passing from reaction 1, and when all the Mo_6Se_8 is transformed in $Cd_1Mo_6Se_8$, a second Cd per formula unit starts to be intercalated as described in reaction (2), therefore only two steps in the potential are present as shown for dashed curve in Figure 2 b). Also CV could be interpreted in the same approach, the first peak corresponds to reaction 1 and the second to reaction 2, both peaks being related to a single intercalation and present similar integrated area.

For fast intercalation (present experiment 0.15 mA for chronopotentiometry and 1mV/s for CV**)**. During galvanostatic intercalation, reaction 1 will happen in the initial period of intercalation but will be rapidly limited to the surface of the Mo_6Se_8 grains, due to the insufficient diffusion of Cd^{2+} in Mo_6Se_8, at such point the potential decreases till it is sufficient to activate reaction 2, but such reaction will cease rapidly once all the limited amount of $Cd_1Mo_6Se_8$ has been consumed. This statement is supported by similar duration for the first two steps of the intercalation at -0.15 mA. Once reaction 2 is terminated, the system is forced to decrease further the potential to activate reaction 3, the direct conversion of

Accepted Manuscript

Mo_6Se_8 into $Cd_2Mo_6Se_8$. Owing to the fact that CV with rapid sweeping time presents three anodic peaks, the first could be ascribed to reaction 1 and it is strongly deformed by the rapid sweep of voltage, the second one, noted as $\mathbf{E_{inta}}$ in figure 1 b) in accordance with galvanostatic intercalation should correspond to the second peak for slow sweeping condition (reaction 2), and finally the third peak should correspond to reaction 3.

For de-intercalation. From a chemistry point of view, for $Cd_xMo_6Se_8$ de-intercalation reactions consist in inverting the reactions discussed in the previous paragraphs. However, based on the physics of transport, it is worth underlining that for intercalation reaction, the front of reaction move from the surface to the center of the crystallites while for de-intercalation the front of the reaction is on the liquid-solid interface. This difference implies that if during galvanostatic de-intercalation the imposed current is higher than the maximum diffusion in the electrode, the surface region will be significantly depleted of Cd compared to the bulk. As the diffusion is depending from the Cd loading in Mo_6X_8, most of the surface results in Cd being depleted, lowering the diffusion, with the consequence to arrive to a kind of trapping mechanism for Cd in the bulk of the electrode. In the de-intercalation experiment at 0.15 mA (red curve Figure 2 b)), in the first two phase region, the $Cd_2Mo_6Se_8$ is oxidized to $Cd_1Mo_6Se_8$ with a rate slightly higher than the Cd diffusion, after the potential increases for the inverse of reaction 1, but the diffusion from the bulk will be also lower and consequently forming a surface layer of Mo_6Se_8 which hinders further oxidation and consequently a significant fraction of $Cd_xMo_6Se_8$ is still present at the end of the de-intercalation. For CV at low sweeping rate, two cathodic peaks are present corresponding to the inverse of reaction 2 and 1 with similar intensity and width whereas for fast sweeping rate the peak corresponding to the inverse of reaction 1 decreases in intensity and increases in width due to the lower diffusion.

Mo_6S_8

Figure 3 shows, in analogy with the work done for selenium phase, a set of diffraction patterns collected *in situ* in the part a and the evolution as function of time of the integrated intensity of a few selected reflections for the different phases as well as the potential. The XRD patterns are also a convolution of up to three phases: the initial binary Mo_6S_8 phase (space group $R\bar{3}$, a=9.19 Å, c=10.89 Å), a first rhombohedral intercalated phase (space group $R\bar{3}$, a=9.41750 Å, c= 10.74200 Å that is ascribed to $Cd_1Mo_6S_8$, and a second rhombohedral

Accepted Manuscript

ternary phase (space group $R\bar{3}$, a=9.82 Å, c=10.57 Å) refined as to $Cd_2Mo_6S_8$ (see below). As in the case of Mo_6Se_8 the rhombohedral setting shows a clearer correlation with Cd stoichiometry with an increase of the cell parameter and the rhombohedral angle: Mo_6S_8 a = 6.43 Å, α= 91.26°, $Cd_1Mo_6S_8$ a = 6.51Å, α =92.63°, $Cd_2Mo_6S_8$ a = 6.67 Å, α =94.74°.

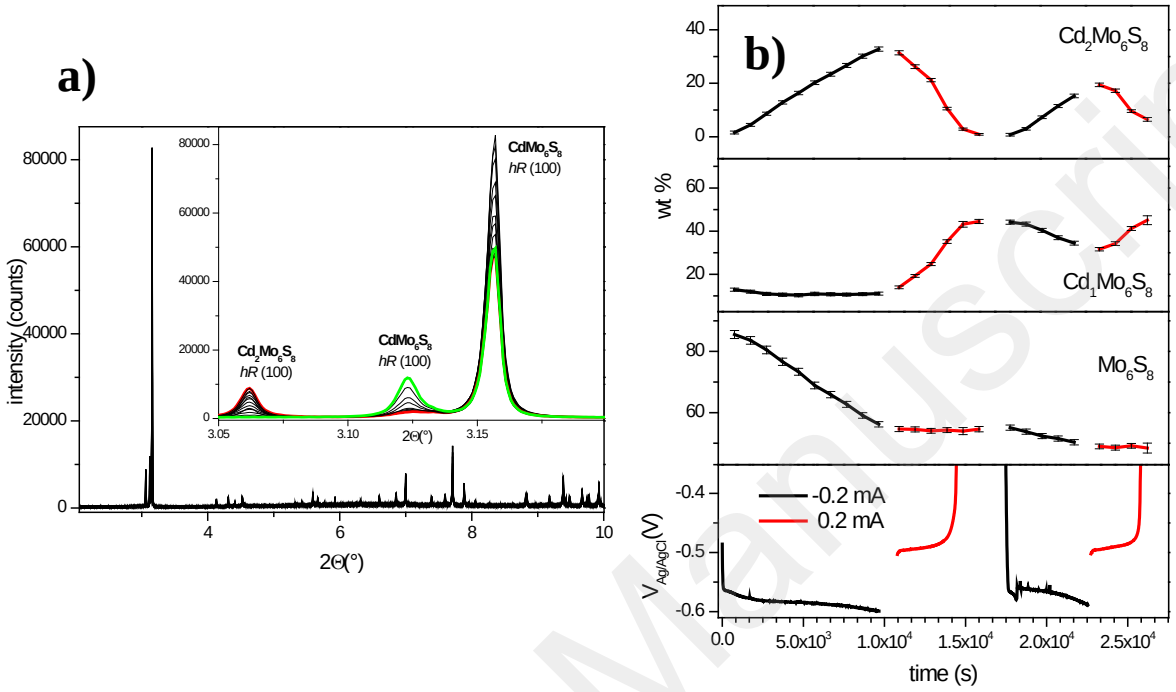


Figure 3 a) Left: typical pattern (inset: zoom around the *hP* (101) reflection of the different phases during the first intercalation stage); part b) from to top to bottom: estimated phase fractions and corresponding voltage evolution as a function of time.

Interestingly although three phases are potentially present as for the Se case, the electrochemistry appears at first sight very different, with only one "*plateau*" present for both intercalation and de-intercalation in accordance with CV where only one cathodic and one anodic peaks are present. Looking in details to the electrochemistry data and to the structural ones, we notice that in the first step of intercalation t <10000 s (in Figure 3 b) the potential stabilizes rapidly around -0.57 V, suggesting a two phase region, this range could be clearly ascribed to reaction (3) with the direct conversion of Mo_6S_8 to $Cd_2Mo_6S_8$.

The de-intercalation process (red curve Figure 3) behaves electrochemically similarly, with another plateau at -0.5 V that lasts for a much shorter time (around 5000 s). However, when looking at the diffraction data, it is clear that this two phase region is not the inverse of the previous intercalation reaction (3), but the inverse of reaction (2), *i.e.*, the conversion of $Cd_2Mo_6S_8$ into $Cd_1Mo_6S_8$. That implies that a Cd trapping effect is present, with the

Accepted Manuscript

irreversible accumulation of Cd in the structure of $CdMo_6S_8$ as proposed by Levi *et al.* [7] . As a consequence, the anodic peak of CV should be ascribed to reaction 2 (or 3 if the sample has never been intercalated) while the cationic peak should be related to the inverse of reaction 2 and not to the reaction 1. This is thus clarifying the Boulanger *et al.*[8] and Gocke *et al.*[23] experiments.

In order to clarify this process, a second intercalation/de-intercalation cycle has been performed. During this second cycle, the main difference is that at the beginning of intercalation, half of Mo_6S_8 has been converted to $Cd_1Mo_6S_8$ from the previous cycle. During intercalation the main reaction is the conversion of $Cd_1Mo_6S_8$ into $Cd_2Mo_6S_8$, during a *plateau* that, although characterized by a strong curvature, could be tentatively defined as -0.55 V. Such value is very close to the intercalation potential of reaction (3) at least in the present experimental configuration, explaining the difficulty to discriminate between the two reactions in the CV. In order to support such attribution, it is possible to use the first cycle, where a small shoulder is present before the *plateau* (time <2000 s) in which the potential is slightly higher and it is possible to notice that the small amount of $Cd_1Mo_6S_8$, created during CV test before interaction, is converted into $Cd_2Mo_6S_8$. For the second de-intecalation cycle, the condition are the same as for the first cycle, although $Cd_1Mo_6S_8$ has a higher concentration and consequently the reaction follows the scheme of the previous one.

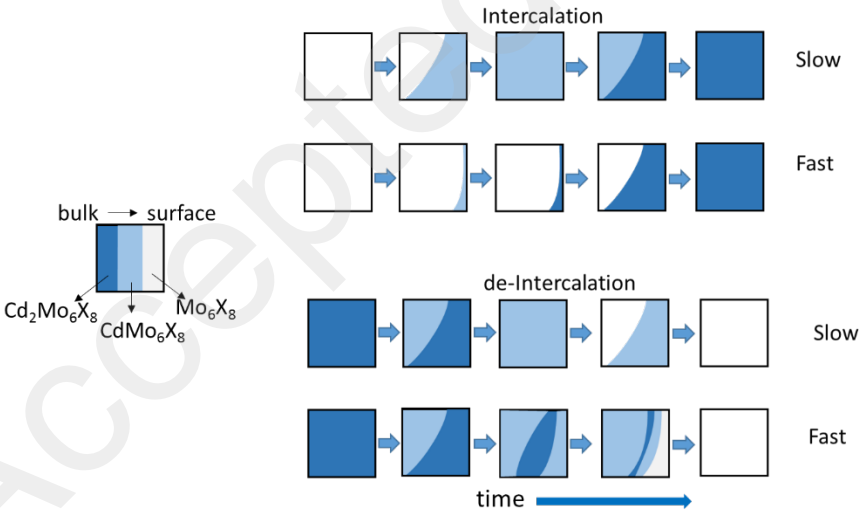


Figure 4: graphical representation of kinetic effect during intercalation and de-intercalation of Cd.

Accepted Manuscript

In a more general approach, the electrochemistry of Mo_6S_8 should be interpreted as an asymptote of an extremely fast experiments for Mo_6Se_8. For instance, in the CV case, the peaks E_{int1}, E_{inta}, E_{deint1} decrease in intensity and broaden as sweep rate is increased. Asymptotically for very fast rate, these peaks will practically disappear and only the peaks E_{int2} and E_{deint2} remain visible. Considering that electrochemical parameters are similar, the current interpretation is that for reaction (1), Cd diffusion in Mo_6S_8 should be several order of magnitude lower than in the case of Mo_6Se_8.

The present model has been graphically depicted in figure 4, it is worth underlining that in the case of fast intercalation the rate determining step will be the diffusion of Cd^{2+} from Mo_6X_8 to $Cd_2Mo_6X_8$ (process (3)) with the later phase continuously replenished by the intercalation. For the fast de-intercalation, the elucidation of the rate determining step is more complex. After a first period in which the surface is completely depleted and an interface of $Cd_1Mo_6X_8$ has been formed between the bulk $Cd_2Mo_6X_8$ phase and the surface, the prosecution of the de-intercalation is limited by the diffusion of Cd^{2+} from $Cd_1Mo_6Se_8$ or $Cd_2Mo_6Se_8$. However, more and more the de-intercalation proceed, more the phase are depleted in Cd and slower is the diffusion. As a consequence, if the diffusion of Cd in Mo_6X_8 is very low, the cation is practically trapped.

Structural analysis

Independently from the chemical composition, the crystal structure of the Chevrel phases is basically the same: a trigonal distorted simple cubic stacking of Mo_6X_8 blocks (Mo_6-octahedral clusters inside an anion cube) forming an open three-dimensional channel system in which cations are hosted. The channels are formed by the association of two types of face-sharing pseudocubic cavities: cavity 1 (blue polyhedra in Figure 5) and cavity 2 (green polyhedra in Figure 5), corresponding to the body centered and the face centered sites of the Mo_6X_8 blocks packing, respectively.

According to the literature[7,39] cation positions are strongly correlated with ionic mobility. on the base of this parameter, the ternary Chevrel phases could be divided in two families: type I were cations are located only near or exactly in the origin of cavity 1, that is the case of large cations with no mobility(like Pb^{2+} for instance) and type II for which cations could be present

Accepted Manuscript

in both cavities and shifted from the center of the cavities as observed for small and mobile cations (like Li^+ for instance). Cd^{2+} has an ionic radius near 1 Å (0.95 Å for coordination number = VI according to R.D. Shannon) as a consequence it is quite difficult to classify it into one of the two classes *a priori*, and structural analysis is mandatory for the understanding of the materials. For such reasons the following sections will be devoted to describe the structures of intercalated phases resulting from Rietveld refinement with particular interest for the positions of Cd^{2+} that have been determined by Fourier difference and successively refined (positions, occupancy and isotropic atomic displacement parameters). In particular, the Cd position will be discussed with the help of electronic density maps obtained by the Maximum Entropy Method (MEM)[40]. In this context, the main advantages of MEM are the possibility to use fully phased data (the phase contribution of Cd is included) and the quality of the density distribution concerning the background, which is usually close to zero and allows the visualization of details, which are inconclusive with standard Fourier techniques.

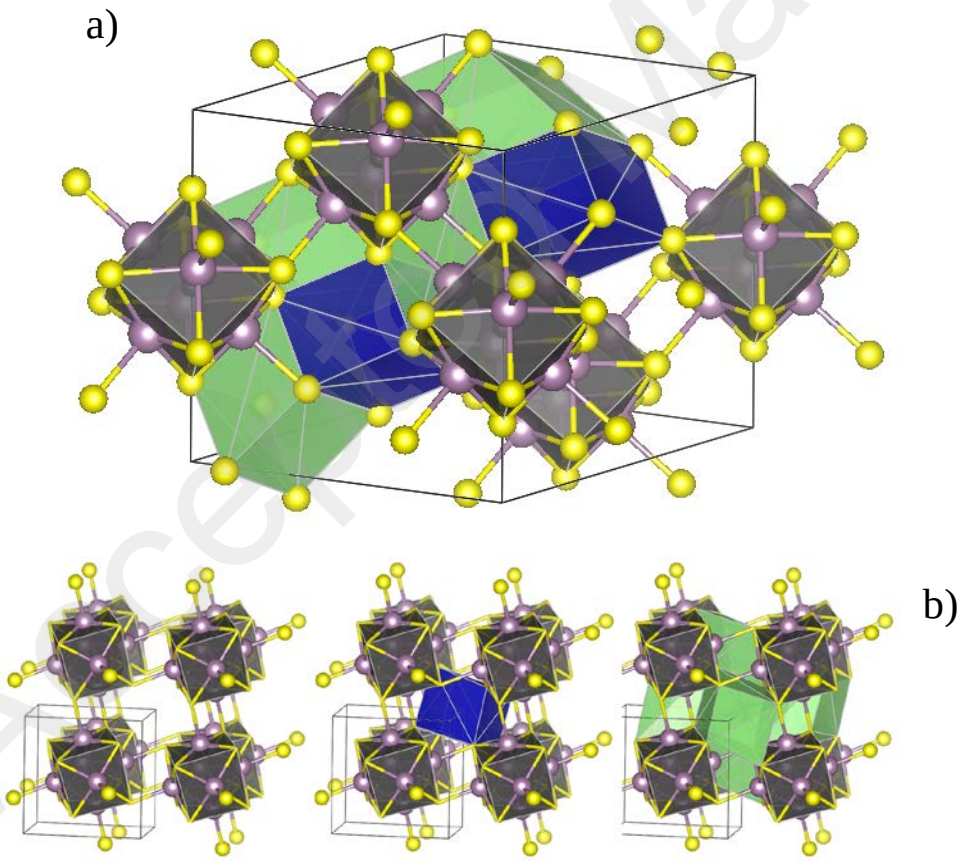


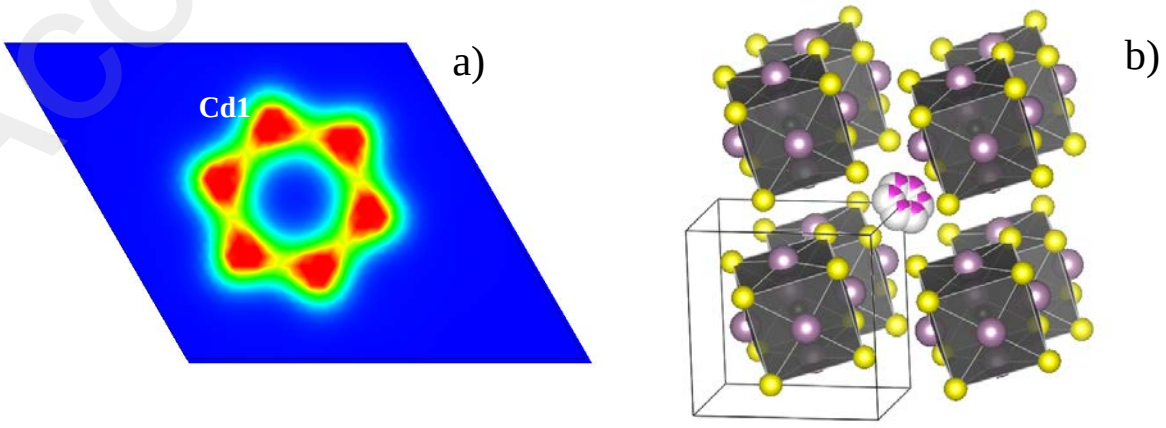
Figure 5: Part a) General structural model for Chevrel phases in hexagonal setting ($R\bar{3}$:*hP*) with cavity 1 and 2, blue and green polyhedra. Part b) Mo_6X_8 blocks simple cubic packing in

Accepted Manuscript

rhombohedral setting ($R\bar{3}$:*hR*) with cavity location.

$Cd_1Mo_6S_8$. As clear from the previous paragraph, it is reasonable to suppose two different models for $Cd_1Mo_6S_8$ crystal structure: the first for which Cd^{2+} is located in the center of cavity 1 in Wyckoff position 3*a* (0.666, 0.333, 0.333) ($R\bar{3}$:*hP*), and a second model, still inside the cavity 1 but with Cd at general position 18*f*. Both models have been used as input for Rietveld refinement of the *ex situ* synchrotron powder diffraction data. However the first model leads to abnormally too huge value for the B_{iso} of Cd. Analysis of Fourier difference map obtained after setting Cd occupancy to zero (Figure S4) shown a residual the electron density within cavity 1 rather centered on the 3*a* site but very diffuse in the *x*,*y* plane. In order to discriminate between the two models, MEM analysis has been applied, as visible in Figure 6, the map obtained shows a clear shift of Cd density from the center of cavity 1, supporting model 2 with Cd at 18*f* position (0.644(9), 0.265(2), 0.333(3) $R\bar{3}$:*hP*) slightly shifted from the 3*a* site (0.57(2) Å).

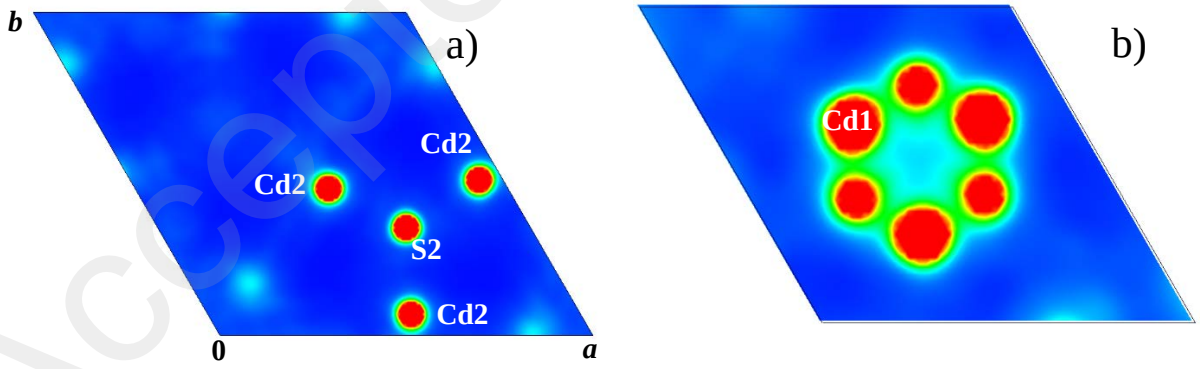
As a consequence, we propose for describing the current data the second model with Cd on the 18*f* general site. Such model is supported by a previous combined neutron and laboratory X-ray powder diffraction study [24] in which Cd has been refined at a very similar position, with a shift of 0.60 Å from the origin. It is worth noticing, that Cd positions generated by symmetry form a six-membered ring in the cavity 1, with a maximum distance between the sites of 1.14 Å, value too small to allow the presence of two Cd in the same cavity 1. Occupancy of Cd was freely refined (its U_{iso} parameter being made identical to the U_{iso} value of Mo) and converged near 1/6 value (0.1598(17)); it implies that each cavity 1 in the structure is fully occupied.



Accepted Manuscript

Figure 6: $Cd_1Mo_6S_8$. Part a) MEM electronic density map within the *a*-*b* plane focused on cavity 1 , *z*= 1/3 (*hP* setting) Max./min. saturation levels at 80/0 $e^{-}\cdot Å^{-3}$. Part b) Graphical representation of the $Cd_1Mo_6S_8$ structure in the (*hR* setting).

$Cd_2Mo_6S_8$. Once $Cd_1Mo_6S_8$ has been classified as a type 2 ternary Chevrel Phase, and as the ionic radius of Cd^{2+} prevents a further occupation of cavity 1, the most reasonable hypothesis is that cavity 2 has to be filled. Indeed, Fourier difference (Figure S5) and MEM (Figure 7 a)) maps obtained after refinement using as starting model the previous crystal structure of $Cd_1Mo_6S_8$ show an additional electron density peak located at position 0.503(5) 0.045(5) 0.464(5) ($R\bar{3}$:*hP*), generating two equivalent sites (around the 9*d* special site at ½ 0 ½) distant from each other by 1.14(11) Å, located in the cavity 2. It is worth underlining that the Cd site in cavity 1 is also strongly modified by the insertion of the second Cd, moving to position 0.606(8) 0.198(5) 0.353(5) and drastically shifted further from the center of the cavity (from 0.57 Å to 1.17 Å). MEM and Fourier difference map clearly show electron density maxima more shifted from the site 3*a* at the center of cavity 1 (see Figure S6 and Figure 7 b)), in respect of the case of $Cd_1Mo_6S_8$. The refinement of the occupancy for Cd in cavity 1 and 2 converges freely to 0.167(8) and 0.187(12), respectively, corresponding to a stoichiometry of $Cd_{2.12}Mo_6S_8$ and an average occupancy of 1.12 and 0.37 for cavity 1 and 2, respectively.



Accepted Manuscript

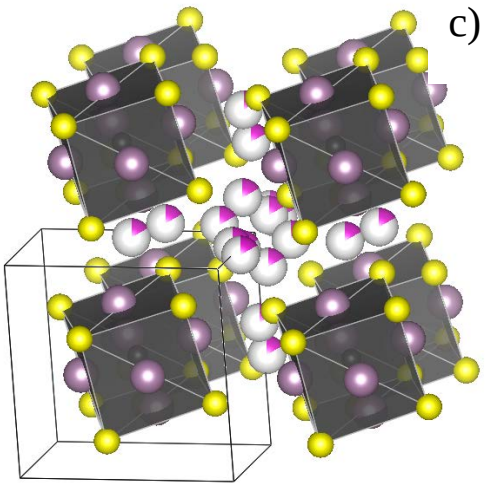


Figure 7: $Cd_2Mo_6S_8$. Part a) Cavity 2: MEM electronic density map within the *a-b* plane at *z*=0.5347 showing three maxima corresponding to the three in-plane Cd2 atoms, shifted from the ideal 9*d* Wyckoff site at ½ 0 ½ (max./min. saturation levels at 8/0 $e^-/Å^{-3}$). Part b) Cavity 1: MEM electronic density map within the *a-b* plane focused on cavity 1, *z*= 0.3472 (*hP* setting). Max./min. saturation levels at 5/0 e $\cdot Å^{-3}$. Part b) Graphical representation of the $Cd_2Mo_6S_8$ structure in the rhombohedral cell.

$Cd_1Mo_6Se_8$. $Cd_1Mo_6Se_8$ has been refined starting from the structural model (site 18*f*) obtained for $Cd_1Mo_6S_8$ achieving satisfactory agreement factors and acceptable U_{iso} values (*R*=3.06%, χ^2=1.63). The position of Cd also turns out to be shifted from the center of cavity 1 to the position 0.65(3) 0.261(8) 0.331(11), which is slightly more shifted from the center of the cavity in respect of $CdMo_6S_8$ (0.64 versus 0.57 Å), with an occupancy of 0.143(11) corresponding to $Cd_{0.86}Mo_6Se_8$. Also in such case the observed density from Fourier difference maps (Figure S7) presents a hugely delocalized apparent maximum on the 3*a* site, but MEM map shows a clear preference for Cd in site 18*f*. The data fitted in accordance with MEM analysis shows a very similar Cd disorder in cavity 1 in both $Cd_1Mo_6S_8$ and $Cd_1Mo_6Se_8$ phases, despite the different anionic lattices (including very close Cd-X distances distribution, ≈0.08 Å longer for Se as expected according to the ionic radii considerations).

Accepted Manuscript

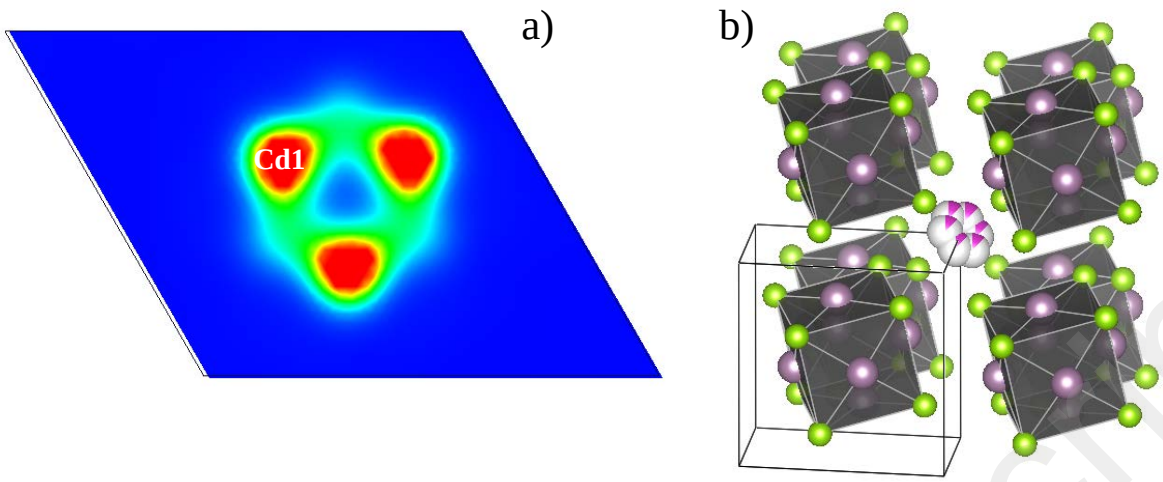
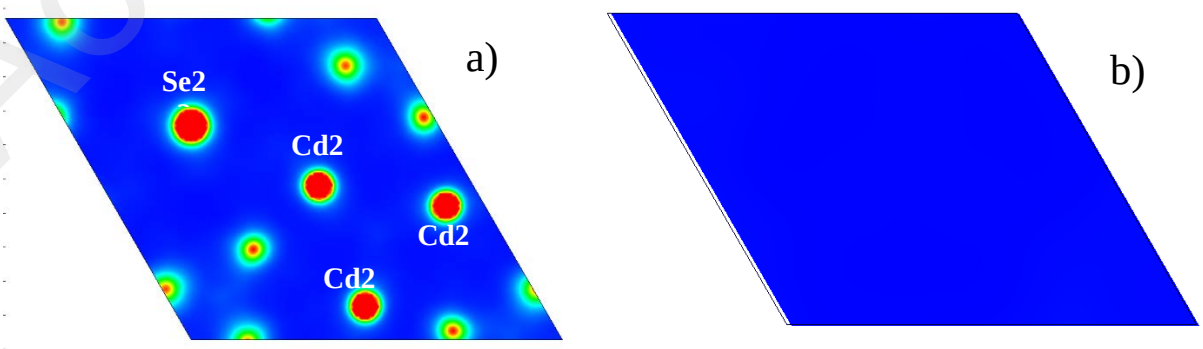


Figure 8: $Cd_1Mo_6Se_8$ Part a) phase, cavity 1: MEM electronic density map within the *a-b* plane centered at 2/3 1/3 0.3194 showing three maxima corresponding to the three in-plane Cd1 atoms (max./min. saturation levels at 30/0 $e^-/Å^{-3}$). Part b) graphical representation of the $Cd_1Mo_6Se_8$ structure in the rhombohedral cell.

$Cd_2Mo_6Se_8$. By analogy with the other Chevrel phases, the starting model used for such phase has been the crystal structure of $Cd_1Mo_6Se_8$ plus an additional site for Cd in a general Wyckoff positon 18*f* inside the cavity 2. However, both Cd sites converged into cavity 2. Fourier difference maps (Figure S8 a)) confirmed that cavity 1 is essentially empty and all the Cd electron density lies within cavity 2 (see Figure 9). For such reasons the fit has been performed finally using a single site in cavity 2 that converged at position 0.518(3) 0.100(2) 0.445(2) with occupancy 0.325(10) corresponding to a stoichiometry of $Cd_{1.95}Mo_6Se_8$. Symmetrically equivalent Cd atoms are separated by 2.24(3) Å within cavity 2, twice the value encountered in cavity 2 of $Cd_2Mo_6S_8$. MEM maps confirmed this cavity occupancy scheme (Fig. 9a) and b)).



Accepted Manuscript

c)

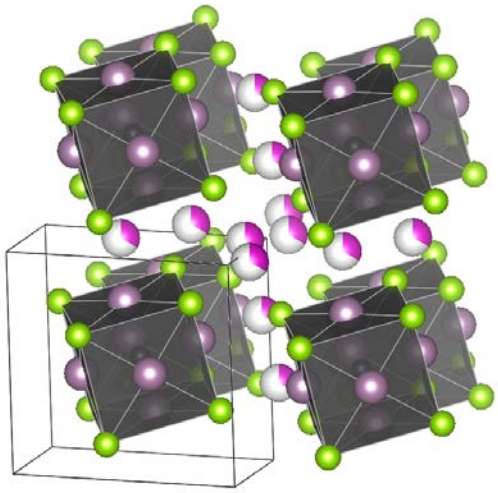


Figure 9: $Cd_2Mo_6Se_8$. Part a) MEM electronic density map within the *a-b* plane at *z*=0.4444 (*hP*) showing three maxima corresponding to the three in-plane Cd2 atoms, shifted from the ideal 9*d* Wyckoff site at ½ 0 ½ (max./min. saturation levels at 10/0 $e^-/Å^{-3}$). Part b) MEM electronic density map within the *a-b* plane centered at 2/3 1/3 0.3194 cavity 1, same zoom, orientation and scale of Figure 8 a). Part c) Graphical representation of the $Cd_2Mo_6Se_8$ structure in the *hR* setting.

Crystal structure of $Cd_2Mo_6Se_8$ is not following the expected scheme of successive occupation of the two cavities, implying also the migration of Cd from cavity 1 to cavity 2 during intercalation. Although unexpected, a similar behavior has been reported for the intercalation of Mg^{2+} in Mo_6Se_8[41], with the two line phases $MgMo_6Se_8$ and $Mg_2Mo_6Se_8$. Although both triclinic, those phases present the same cavity filling scheme as observed in the trigonal $Cd_2Mo_6Se_8$ phase. In this context, it is worth noticing that such similarity between the two cations is maintained also for Sulphur phases. $MgMo_6S_8$ has a trigonal structure with Mg hosted in cavity 1 at 0.90(3) Å from its center, that presents also some trapping character, further intercalation form the trigonal $Mg_2Mo_6S_8$ that, as for $Cd_2Mo_6S_8$, hosts the additional Mg in the cavity 2 (18*f* site) and the site in the cavity 1 moves further away from the center (1.117(18) Å from site 3*a*).

In order to better understand the intercalation chemistry of Cd into the Chevrel phases, Bond valence sum (BVS) and Bond valence site energy (BVSE) maps have been calculated for the four intercalated ternary structures. BVSE is a method derived from bond valence sum [42] that

Accepted Manuscript

combines the bond valence sum mismatch map in a form of a Morse potential with a cation-cation electrostatic repulsion term. It presents as main advantage, compared to bond valence sum mismatch map, an energy scale that could be compared with atomistic calculations and a more accurate treatment of the sites near other cations. However, it is worth noticing that in the specific case of transition metal cluster compounds the results must be considered only due to the difficulties to treat in such simple approximation the cluster charges and lattice strain effects [43]. The obtained map for selenium are visible in Figure 10, and the method is able to reproduce the main features of the experiments such as the lowest conductivity and preferential occupation of cavity 1 for $Cd_1Mo_6X_8$ or the stabilization of the site in cavity 2 accompanied by an increase of shift from the center of the cavity 1 for $Cd_2Mo_6X_8$ although the BVSE doesn't show a clear inversion of stability between the two sites for $Cd_2Mo_6Se_8$.

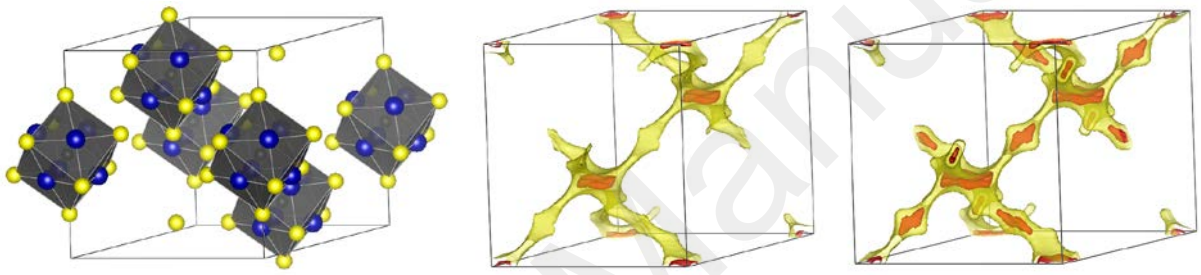


Figure 10: Part a) Chevrel phases in hexagonal setting ($R\bar{3}$:*hP*), BVSE map for $Cd_1Mo_6Se_8$ and $Cd_2Mo_6Se_8$ part b) and c), respectively. Red and yellow isosurfaces corresponds to 0.3 and 0.5 eV above the minimum and the percolation energy, respectively.

Due to the relatively good agreement of such method, it is of interest to consider separately the two main components of the BVSE: valence mismatch and coulomb interaction. Effectively the BVS clearly shows that the site on cavity 2 presents a higher valence mismatch also for $Cd_2Mo_6X_8$ phases (estimated valence around 2.5 and 2.0 for cavity 2 and 1, respectively) although in the BVSE map the two sites result with a similar stability. As a consequence, the stabilization of the cavity 2 for BVSE method in $Cd_2Mo_6X_8$ should be ascribed to Mo-Cd repulsion. Actually, the use of a higher oxidation state for Mo in BVSE calculation results in a further stabilization of cavity 1. In this approximation, excluding a direct covalent interaction between the cluster and Cd^{2+} due to the relatively long distance between Mo and Cd, the key parameter for the stabilization of cavity 2 is the actual charge on the cluster that is in turn dependent from the electron count but also to steric effects[43]. The

Accepted Manuscript

variation of the cluster geometry during the intercalation could be used as indirect indicator of the cluster charge, and effectively it could be noticed that cluster apical distance is almost independent from the anion for Mo_6X_8 (X=Se: 3.9087(12) Å, X=S: 3.9346(11) Å) and $CdMo_6X_8$ (X=Se: 3.842(7) Å, X=S: 3.844(7) Å but not for Cd_2MoX_8 (X=Se: 3.790(14) Å , X=S: 3.73(2) Å) for which the cavity occupation scheme is different.

It is worth underlining that the different cavities occupations for $Cd_2Mo_6X_8$ have a fundamental consequence in ionic transport mechanism. Effectively, although the topology of the percolation paths remain the same **pcu** type, the availability of unoccupied nodes during cationic transport changes drastically. For instance, in the case of $Cd_2Mo_6S_8$, Cd hopping is formally hindered by the full average occupancy of cavity 1, implying locally a vacancy mechanism of ionic conduction, while in the case of $Cd_2Mo_6Se_8$, two empty cavities 2 over the six connected to the closest empty cavity 1 are always available for Cd hopping.

Conclusion

In the present work the electrochemical intercalation/de-intercalation of Cd into the Chevrel phases Mo_6X_8 (X=S, Se) has been studied *in situ*, and the crystal structure of the intercalated phases so obtained has been determined. The processes of the electrochemical Cd insertion into the host material Mo_6X_8 occurred stepwise, involving only two separate phases $Cd_1Mo_6X_8$ and $Cd_2Mo_6X_8$, although the electrochemical characterization shows a more complex picture than debated in the past[7,8,23,36]. Effectively, the coupling of *in situ* X-ray powder diffraction and electrochemical measurements has allowed to reveal a strong dependency of the process from the imposed electrochemistry kinetics, mainly dependent on the less common increase of ionic conductivity during intercalation, in particular the competition for the formation of $Cd_2Mo_6X_8$ between the two step ($Mo_6X_8 \rightarrow CdMo_6X_8 \rightarrow Cd_2Mo_6X_8$) and the single step ($Mo_6X_8 \rightarrow Cd_2Mo_6X_8$) intercalation processes or the trapping mechanism for $CdMo_6S_8$.

Ex situ synchrotron X-ray Rietveld refinement of samples in various stage of intercalation has allowed to determine the structure of $Cd_2Mo_6X_8$ phases previously unknown. The $Cd_2Mo_6Se_8$ shows an unexpected structure, in which Cd is hosted integrally in the cavity 2, in opposition to the classical scheme [7,39] and to the structure of the isostoichiometric $Cd_2Mo_6S_8$. Such variation in cavity stability cannot be rationalized only with valence misfit calculated by BVS; BVSE calculations suggest that also coulomb interaction should be taken in account and the

Accepted Manuscript

stabilization of cavity 2 should be related with the actual charge on the Mo cluster. The different cavity filling scheme for $Cd_2Mo_6Se_8$ implies a different transport mechanism that could have strong effect on conductivity and applications.

The results shown in this work should be an important basis for a better understanding of the electrochemical intercalation reaction of divalent ions into Mo_6X_8 phases and an useful indication for device development that are founded on such processes.

ASSOCIATED CONTENT

Supplementary figures (PDF), including experimental setup, Rietveld refinements and Fourier differences.

Detailed crystallographic information (CIF files), copy of the CIF files are available on ICS database codes:

1864057 Cd1Mo6S8
1864019 Cd2Mo6S8
1864058 Cd1Mo6Se8
1864021 Cd2Mo6Se8

■ ACKNOWLEDGMENTS

Authors would like to warmly thank Dr. Patrick Gougeon for his expert advices and the solid state synthesis of the binary Chevrel phases. We acknowledge the European Synchrotron Radiation Facility for provision of synchrotron radiation facilities and we would like to thank Dr. Andy Fitch for his valuable scientific and technical assistance during experiment and making available data transfer facilities. Mr Christophe Derouet is warmly acknowledged for his technical assistance in the fabrication of the electrochemical cell for *in situ* experiments.

Accepted Manuscript

References

(1) Chevrel, R.; Sergent, M.; Prigent, J. Sur de Nouvelles Phases Sulfurées Ternaires Du Molybdène. *J. Solid State Chem.* **1971**, *3* (4), 515–519.

(2) Schöllhorn, R.; Kümpers, M.; Lerf, A.; Umlauf, E.; Schmidt, W. Structure and Superconductivity of Ternary Chalcogenides $Cu_xMo_6S_8$ Prepared by Topotactic Electrode Reactions. *Mater. Res. Bull.* **1979**, *14* (8), 1039–1047.

(3) Schöllhorn, R. Reversible Topotactic Redox Reactions of Solids by Electron/Ion Transfer. *Angew. Chem. Int. Ed. Engl.* **1980**, *19* (12), 983–1003.

(4) Aurbach, D.; Lu, Z.; Schechter, A.; Gofer, Y.; Gizbar, H.; Turgeman, R.; Cohen, Y.; Moshkovich, M.; Levi, E. Prototype Systems for Rechargeable Magnesium Batteries. *Nature* **2000**, *407* (6805), 724–727.

(5) Seghir, S.; Boulanger, C.; Diliberto, S.; Lecuire, J.-M.; Potel, M.; Merdrignac-Conanec, O. Electrochemical Reactions of Reversible Intercalation in Chevrel Compounds for Cationic Transfer – Principle and Application on Co^{2+} Ion. *Electrochem. Commun.* **2008**, *10* (10), 1505–1508.

(6) Seghir, S.; Boulanger, C.; Diliberto, S.; Potel, M.; Lecuire, J.-M. Selective Transfer of Cations between Two Electrolytes Using the Intercalation Properties of Chevrel Phases. *Electrochimica Acta* **2010**, *55* (3), 1097–1106.

(7) Levi, E.; Gershinsky, G.; Aurbach, D.; Isnard, O.; Ceder, G. New Insight on the Unusually High Ionic Mobility in Chevrel Phases. *Chem. Mater.* **2009**, *21* (7), 1390–1399.

(8) Boulanger, C.; Lecuire, J. M. Molybdenum Cluster Chalcogenide Electrochemistry—3. Study of Cadmium Insertion into the Host-Lattices Mo_yX_Z. *Electrochimica Acta* **1988**, *33* (11), 1573–1579.

(9) Kaidi, Z.; Boulanger, C.; Lecuire, J. M.; Lemée, N.; Guilloux-Viry, M.; Perrin, A. Ternary Molybdenum Cluster Sulfides: Electrochemical and Chemical Behavior of in Situ Pulsed Laser Deposited Thin Films. *Solid State Sci.* **1999**, *1* (7), 623–635.

(10) Boursicot, S.; Bouquet, V.; Bombard, A.; Langer, M.; Boulanger, C.; Guilloux-Viry, M. Electrochemical Behaviour of $Cu_xMo_6S_8$ Thin Films Synthesized by CSD. *Electrochimica Acta* **2017**, *257*, 436–443.

(11) Smeu, M.; Hossain, M. S.; Wang, Z.; Timoshevskii, V.; Bevan, K. H.; Zaghib, K. Theoretical Investigation of Chevrel Phase Materials for Cathodes Accommodating Ca^{2+} Ions. *J. Power Sources* **2016**, *306*, 431–436.

(12) Mei, L.; Xu, J.; Wei, Z.; Liu, H.; Li, Y.; Ma, J.; Dou, S. Chevrel Phase Mo_6T_8 (T = S, Se) as Electrodes for Advanced Energy Storage. *Small* **2017**, *13* (34), 1701441.

(13) Hebié, S.; Alloin, F.; Iojoiu, C.; Berthelot, R.; Leprêtre, J.-C. Magnesium Anthracene System-Based Electrolyte as a Promoter of High Electrochemical Performance Rechargeable Magnesium Batteries. *ACS Appl. Mater. Interfaces* **2018**, *10* (6), 5527–5533.

(14) Murgia, F.; Antitomaso, P.; Stievano, L.; Monconduit, L.; Berthelot, R. Express and Low-Cost Microwave Synthesis of the Ternary Chevrel Phase $Cu_2Mo_6S_8$ for Application in Rechargeable Magnesium Batteries. *J. Solid State Chem.* **2016**, *242*, 151–154.

(15) Guyot, E.; Seghir, S.; Diliberto, S.; Lecuire, J.-M.; Boulanger, C. Lithium Recovery by Electrochemical Transfer Junction Based on Intercalation Host Matrix. *Electrochem. Commun.* **2012**, *23*, 29–32.

(16) Boulanger, C.; Seghir, S.; Leclerc, N.; Diliberto, S.; Lecuire, J.-M. Method and Device for Selective Cation Extraction by Electrochemical Transfer in Solution and Applications of Said Method. US8449747B2, May 28, 2013.

(17) Li, J.-T.; Baker, A. J. M.; Ye, Z.-H.; Wang, H.-B.; Shu, W.-S. Phytoextraction of Cd-Contaminated Soils: Current Status and Future Challenges. *Crit. Rev. Environ. Sci. Technol.* **2012**, *42* (20), 2113–2152.

(18) McLaughlin, M. J.; Parker, D. R.; Clarke, J. M. Metals and Micronutrients – Food Safety Issues. *Field Crops Res.* **1999**, *60* (1), 143–163.

Accepted Manuscript

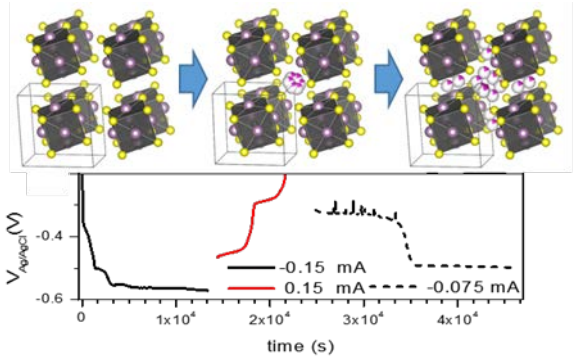
(19) Smeets, K.; Ruytinx, J.; Semane, B.; Van Belleghem, F.; Remans, T.; Van Sanden, S.; Vangronsveld, J.; Cuypers, A. Cadmium-Induced Transcriptional and Enzymatic Alterations Related to Oxidative Stress. *Environ. Exp. Bot.* **2008**, *63* (1), 1–8.
(20) Sasaki, K.; Yongvongsoontorn, N.; Tawarada, K.; Ohnishi, Y.; Arakane, T.; Kayama, F.; Abe, K.; Oguma, S.; Ohmura, N. Cadmium Purification and Quantification Using Immunochromatography. *J. Agric. Food Chem.* **2009**, *57* (11), 4514–4519.
(21) Woodard, F.; Woodard & Curran, I. *Industrial Waste Treatment Handbook*; Elsevier/Butterworth-Heinemann: Amsterdam; Boston, 2006.
(22) Boulanger, C.; Lecuire, J. M. Molybdenum Cluster Chalcogenide Electrochemistry—2. Determination of the Insertion System Normal Potentials from the Analysis of the i = f(E) Curves in the Potentiodynamic Way. *Electrochimica Acta* **1988**, *33* (11), 1567–1571.
(23) Gocke, E.; Schramm, W.; Dolscheid, P.; Schöllhorn, R. Molybdenum Cluster Chalcogenides Mo_6X_8: Electrochemical Intercalation of Closed Shell Ions Zn^{2+}, Cd^{2+}, and Na. *J. Solid State Chem.* **1987**, *70* (1), 71–81.
(24) Tarascon, J. M.; Hull, G. W.; Marsh, P.; Haar, T. Electrochemical, Structural, and Physical Properties of the Sodium Chevrel Phases $Na_xMo_6X_{8-y}I_y$ (X = S, Se and y = 0 to 2). *J. Solid State Chem.* **1987**, *66* (2), 204–224.
(25) Chae, M. S.; Heo, J. W.; Lim, S.-C.; Hong, S.-T. Electrochemical Zinc-Ion Intercalation Properties and Crystal Structures of $ZnMo_6S_8$ and $Zn_2Mo_6S_8$ Chevrel Phases in Aqueous Electrolytes. *Inorg. Chem.* **2016**, *55* (7), 3294–3301.
(26) Lee, B.; Lee, H. R.; Yim, T.; Kim, J. H.; Lee, J. G.; Chung, K. Y.; Cho, B. W.; Oh, S. H. Investigation on the Structural Evolutions during the Insertion of Aluminum Ions into Mo_6S_8 Chevrel Phase. *J. Electrochem. Soc.* **2016**, *163* (6), A1070–A1076.
(27) Fischer, C.; Gocke, E.; Stege, U.; Schöllhorn, R. Molybdenum Cluster Chalcogenides: In Situ X-Ray Studies on the Formation of $Cu_xMo_6S_8$ via Electron/Ion Transfer. *J. Solid State Chem.* **1993**, *102* (1), 54–68.
(28) Levi, E.; Gershinsky, G.; Aurbach, D.; Isnard, O. Crystallography of Chevrel Phases, MMo_6T_8 (M = Cd, Na, Mn, and Zn, T = S, Se) and Their Cation Mobility. *Inorg. Chem.* **2009**, *48* (18), 8751–8758.
(29) Hodeau, J.-L.; Bordet, P.; Anne, M.; Prat, A.; Fitch, A. N.; Dooryhee, E.; Vaughan, G.; Freund, A. K. Nine-Crystal Multianalyzer Stage for High-Resolution Powder Diffraction between 6 KeV and 40 KeV; Macrander, A. T., Freund, A. K., Ishikawa, T., Mills, D. M., Eds.; San Diego, CA, USA, 1998; p 353.
(30) Rodríguez-Carvajal, J. Recent Advances in Magnetic Structure Determination by Neutron Powder Diffraction. *Phys. B Condens. Matter* **1993**, *192* (1–2), 55–69.
(31) Petříček, V.; Dušek, M.; Palatinus, L. Crystallographic Computing System JANA2006: General Features. *Z. Für Krist. - Cryst. Mater.* **2014**, *229* (5), 345–352.
(32) Momma, K.; Ikeda, T.; Belik, A. A.; Izumi, F. Dysnomia, a Computer Program for Maximum-Entropy Method (MEM) Analysis and Its Performance in the MEM-Based Pattern Fitting. *Powder Diffr.* **2013**, *28* (3), 184–193.
(33) Momma, K.; Izumi, F. VESTA 3 for Three-Dimensional Visualization of Crystal, Volumetric and Morphology Data. *J. Appl. Crystallogr.* **2011**, *44* (6), 1272–1276.
(34) Cordero, B.; Gómez, V.; Platero-Prats, A. E.; Revés, M.; Echeverría, J.; Cremades, E.; Barragán, F.; Alvarez, S. Covalent Radii Revisited. *Dalton Trans.* **2008**, No. 21, 2832.
(35) Belin, S.; Chevrel, R.; Sergent, M. Single Crystal Structural Investigations on $Ni_yMo_6Se_{8-x}S_x$ Solid Solution: A New Location of Nickel Counterions. *J. Solid State Chem.* **2000**, *155* (1), 250–258.
(36) Boulanger, C.; Lecuire, J. M. Molybdenum Cluster Chalcogenide Electrochemistry—1. Potentiodynamic Study of Topotactic Insertion Reactions. *Electrochimica Acta* **1988**, *33* (11), 1561–1565.
(37) Levi, E.; Gofer, Y.; Vestfreed, Y.; Lancry, E.; Aurbach, D. $Cu_2Mo_6S_8$ Chevrel Phase, A Promising Cathode Material for New Rechargeable Mg Batteries: A Mechanically Induced Chemical Reaction. *Chem. Mater.* **2002**, *14* (6), 2767–2773.

Accepted Manuscript

(38) Armand, M. B. Intercalation Electrodes. In *Materials for Advanced Batteries*; Murphy, D. W., Broadhead, J., Steele, B. C. H., Eds.; NATO Conference Series; Springer US: Boston, MA, 1980; pp 145–161.
(39) *Superconductivity in Ternary Compounds II*; Maple, M. B., Fischer, Ø., Eds.; Topics in Current Physics; Springer Berlin Heidelberg: Berlin, Heidelberg, 1982; Vol. 34.
(40) Kumazawa, S.; Kubota, Y.; Takata, M.; Sakata, M.; Ishibashi, Y. MEED: A Program Package for Electron-Density-Distribution Calculation by the Maximum-Entropy Method. *J. Appl. Crystallogr.* **1993**, *26* (3), 453–457.
(41) Levi, E.; Mitelman, A.; Isnard, O.; Brunelli, M.; Aurbach, D. Phase Diagram of Mg Insertion into Chevrel Phases, $Mg_xMo_6T_8$ (T = S, Se). 3. The Crystal Structure of Triclinic $Mg_2Mo_6Se_8$. *Inorg. Chem.* **2008**, *47* (6), 1975–1983.
(42) Adams, S. Practical Considerations in Determining Bond Valence Parameters. In *Bond Valences*; Brown, I. D., Poeppelmeier, K. R., Eds.; Springer Berlin Heidelberg: Berlin, Heidelberg, 2013; Vol. 158, pp 91–128.
(43) Levi, E.; Aurbach, D.; Isnard, O. Bond-Valence Model for Metal Cluster Compounds. I. Common Lattice Strains. *Acta Crystallogr. Sect. B Struct. Sci. Cryst. Eng. Mater.* **2013**, *69* (5), 419–425.

Accepted Manuscript

For Table of Contents Only



Synopsis:

The chemistry of electrochemical intercalation of Cd^{2+} in Chevrel phase has been investigated by combined synchrotron X-ray powder diffraction and electrochemistry. The crystal structure of $Cd_2Mo_6X_8$ (X=S, Se) phases, only synthesizable by a topotactic intercalation, has been determined, showing for $Cd_2Mo_6Se_8$ a novel trigonal structure with only cavity 2 occupied.

Accepted Manuscript